

Moiré Strain Skyrmions in Sliding Twisted Bilayers

Rong Hu, Yu-Tao Tan, Dapeng Liu, Jie Ren,* and Yizhou Liu*

*Center for Phononics and Thermal Energy Science, China-EU Joint Lab on Nanophononics,
School of Physics Science and Engineering, Tongji University, 200092 Shanghai, China*

E-mail: xonics@tongji.edu.cn; yizhouliu@tongji.edu.cn

Abstract

Strain defect is crucial to the physical properties of solid materials. Among them, strain glass induced by defect engineering provides an important paradigm for nanoscale domain manipulation. Here, we propose purely mechanical moiré strain Skyrmions, a topologically protected elastic textures whose motion can be controlled by interlayer sliding and the chirality of the moiré bilayer. Using an empirical continuum elastic model combined with symmetry analysis, we demonstrate the Skyrmion lattice structure as the elastic ground state. Under interlayer sliding, these moiré strain Skyrmions exhibit the Skyrmion Hall effect of transverse motion, with a Hall angle determined by bilayer chirality and inversely proportional to the moiré twist angle. Our work establishes interlayer sliding as an efficient, low-energy control knob for topological excitations, offering a new paradigm for designing chiral-material-based information transport devices.

Keywords: Strain defect, moiré system, strain Skyrmion, Skyrmion Hall effect, continuum elastic model

Introduction

The strain defect serves as a powerful inducer for tuning the physical, chemical, and electronic properties of solid-state materials.¹⁻⁷ In crystalline solids, strain defects arise from a range of sources, such as dislocations,⁸⁻¹⁰ point defects,¹¹⁻¹³ grain boundaries^{8,14} and lattice mismatches.^{15,16} Strain fields are a type of lattice defects, in two-dimensional(2D) materials, strain defects acquire particular significance due to its abnormal properties,⁷ such as altering electron-phonon coupling,¹⁷ reshaping energy band,^{5,7} superconductivity¹⁷ and so on. Consequently, the ability to manipulate strain defects through external stimulation affords precise control over material functionalities, making strain defects a cornerstone of modern materials design for smart and adaptive systems.

In recent years, the discovery of several exotic strain-induced phase transition phenomena has fundamentally overturned our understanding of phase of elastic matter. Notably, the strain glass state—a disordered state of frozen martensitic nanodomains—was first reported in 2005 by Sarkar et al¹⁸ and has since been extensively investigated.^{19,20} This unique state exhibits many intriguing physical properties, including high mechanical strength,²¹ large piezoelectric responses,²² switchable ferroelectricity,²³ and a colder-is-faster transition behavior that contrasts with traditional oxide and metallic glasses.²⁴ The strain glass paradigm has broadened the theory of phase transformations in ferroelastic systems, which provides new avenues for nanodomain engineering. However, artificially engineering such as phase necessitates a platform where long-range periodic frustration naturally replaces the role of random defects in stabilizing these nanoscale domains. In parallel, the rapid development of topological phononics has revealed that lattice vibrations and elastic deformations can also exhibit rich topological properties, including spin in acoustics,²⁵⁻³² phonon edge state^{33,34} and chiral phonon transport.³⁵⁻³⁷ In particular, recent advances in quantum phononics have demonstrated that phonon spin and chirality can serve as new degrees of freedom for manipulating mechanical information, opening up exciting possibilities for chiral mechanical devices.³⁸⁻⁴⁰

In this work, we propose a controllable topological strain phase, the strain Skyrmion lattice, in twisted bilayer graphene (TBG), wherein the Skyrmion lattice sites are highly tunable via in-

terlayer sliding as shown in Fig. 1. Based on an continuum elastic model incorporating both in-plane and out-of-plane degrees of freedom, we find that the ground-state displacement field of each layer, with respect to the untwisted case, exhibits a topological structure characterized by quantized Skyrmion number within each moiré supercell thus forming a strain Skyrmion triangular lattice. Furthermore, we demonstrate that by introducing interlayer sliding adiabatically, the strain Skyrmions exhibit a topological Skyrmion Hall effect with the Hall angle (i.e. the ratio between the Skyrmion drift speed v_s and the interlayer sliding speed v_0) controlled by the twist angle of the moiré lattice. We further generalize the strain Skyrmion Hall effect to arbitrary moiré systems with point group symmetries C_n ($n = 2, 3, 4, 6$). This work establishes a theoretical foundation for the mechanical manipulation of topological strain quasiparticles, opening new avenues for designing chiral material devices and high-speed, mechanically driven information transport architectures.

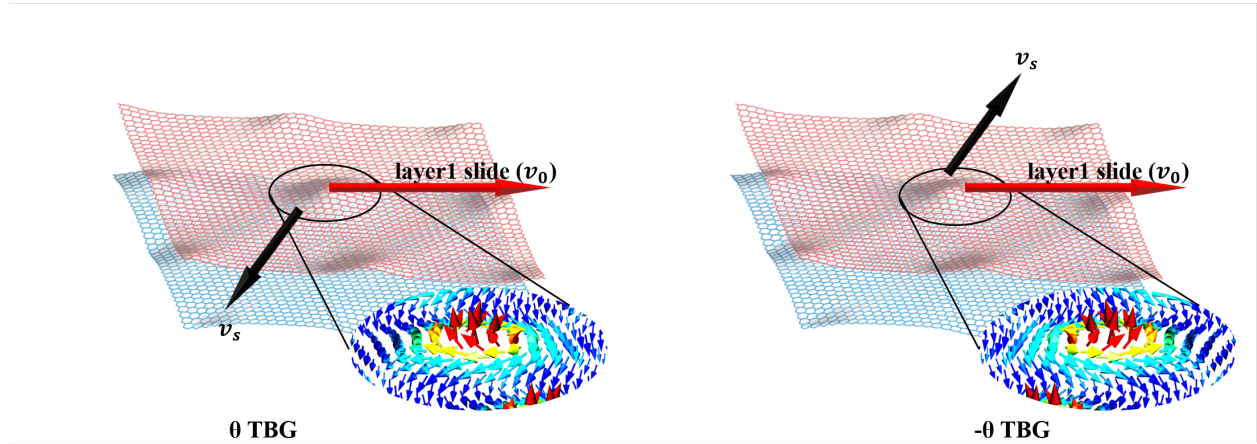


Figure 1: Strain Skyrmion Hall effect induced by interlayer sliding in twisted bilayer graphene (TBG). Left panel: Under a counter-clockwise twist angle (θ), the drift velocity of the skyrmion (\mathbf{v}_s) is proportional to the sliding velocity (\mathbf{v}_0), showing a positive linear Hall conductivity, i.e. $v_s^x = \sigma_{xy} v_0^y$ with $\sigma_{xy} > 0$. Right panel: Under a clockwise twist angle ($-\theta$), the Hall conductivity becomes negative.

Strain Skyrmion in Ground State of TBG

We consider a TBG lattice with a relatively small twist angle θ , typically a few degrees. Under the condition, the wavelength of the moiré system is far larger than the lattice constant, justifying

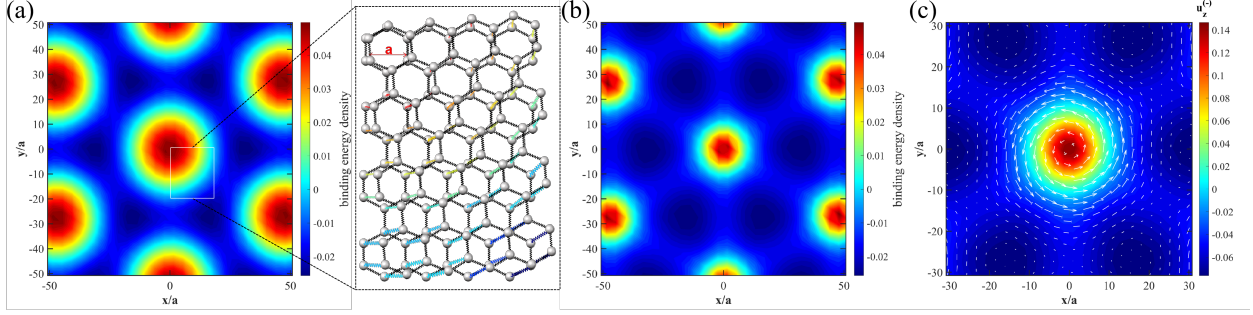


Figure 2: (a) Real-space distribution of interlayer binding energy U_B before relaxation in twisted bilayer graphene (TBG). The right panel shows a zoom-out real-space atomic structure of TBG. The red (blue) colored springs represent higher (lower) interlayer binding energy. (b) Real-space distribution of U_B after relaxation in TBG. (c) The relaxation displacement field of the TBG, with white arrows indicating in-plane components ($u_{x,y}^{(-)} = u_{x,y}^{(2)} - u_{x,y}^{(1)}$) and the background color represents the out-of-plane component ($u_z^{(-)} = u_z^{(2)} - u_z^{(1)}$). $\mathbf{u}^{(-)} = \mathbf{u}^{(2)} - \mathbf{u}^{(1)}$ represents the interlayer relative displacement field vector. This displacement field can be characterized by a topological Skyrmion number $N = 1$.

the use of a continuous elastic model. We introduce the displacement field $\mathbf{u}^{(l)} = (u_x^{(l)}, u_y^{(l)}, u_z^{(l)})$ to describe in-plane and out-of-plane displacement terms of l th layer ($l \in \{1, 2\}$). We further define the symmetric and antisymmetric displacement combinations as $\mathbf{u}^{(\pm)} = \mathbf{u}^{(2)} \pm \mathbf{u}^{(1)}$. The total elastic energy of the TBG system can be decomposed into an intralayer term and an interlayer binding energy term. The intralayer term comprises a standard elastic term, expressed as $U_E = \sum_{l=1}^2 \sum_{\alpha,\beta=x,y} \int d^2\mathbf{r} [\frac{\lambda}{2}(\partial_\alpha u_\alpha^{(l)})^2 + \frac{\mu}{4}(\partial_\alpha u_\beta^{(l)} + \partial_\beta u_\alpha^{(l)})^2] = \sum_{\alpha,\beta=x,y} \int d^2\mathbf{r} \frac{\lambda}{4}[(\partial_\alpha u_\alpha^{(+)})^2 + (\partial_\alpha u_\alpha^{(-)})^2] + \frac{\mu}{8}[(\partial_\alpha u_\beta^{(+)} + \partial_\beta u_\alpha^{(+)})^2 + (\partial_\alpha u_\beta^{(-)} + \partial_\beta u_\alpha^{(-)})^2]$, where $\mu \approx 9.57 \text{ eV}\text{\AA}^{-2}$ and $\lambda \approx 3.25 \text{ eV}\text{\AA}^{-2}$ are the Lamé coefficients of the monolayer graphene.⁴¹ The interlayer binding energy (U_B) consists of an in-plane term (U_B^\parallel) and an out-of-plane term (U_B^\perp), i.e. $U_B = U_B^\parallel + U_B^\perp$, where U_B^\parallel is expressed as $U_B^\parallel = \sum_{j=1}^3 \int V_0 \cos[\mathbf{G}_j^M \cdot \mathbf{r} + \mathbf{a}_j^* \cdot \mathbf{u}^{(-)}] d^2\mathbf{r}$.⁴¹⁻⁴³ \mathbf{a}_j^* ($j = 1, 2, 3$) are the reciprocal lattice vectors corresponding to primitive graphene: $\mathbf{a}_1^* = \frac{4\pi}{\sqrt{3}a}(\frac{\sqrt{3}}{2}, -\frac{1}{2}, 0)$, $\mathbf{a}_2^* = \frac{4\pi}{\sqrt{3}a}(0, 1, 0)$, and $\mathbf{a}_3^* = -\mathbf{a}_1^* - \mathbf{a}_2^*$ (a is the lattice constant); \mathbf{G}_j^M are the corresponding reciprocal lattice vectors of moiré supercell: $\mathbf{G}_j^M = [1 - R_z(-\theta)]\mathbf{a}_j^*$ ($R_z(\cdot)$ refers to the rotation operation along z axis). The out-of-plane term is expressed as

$$U_B^\perp = \int d^2\mathbf{r} C[u_z^{(-)} + \bar{d} - d_{\text{opt}}]^2, \quad (1)$$

where C is a constant, \bar{d} refers to the interlayer distance of untwisted bilayer graphene, and d_{opt} is the optimized interlayer distance in the presence of interlayer twist. We assume that the optimized interlayer distance is given by

$$d_{\text{opt}} = \bar{d} + \sum_{j=1}^3 \frac{2}{9} \Delta d \cos[\mathbf{G}_j^M \cdot \mathbf{r} + \mathbf{a}_j^* \cdot \mathbf{u}^{(-)}], \quad (2)$$

where the maximum value of d_{opt} is $d_{\text{opt}}^{\text{max}} = \bar{d} + \frac{2}{3} \Delta d$ and the minimum value is $d_{\text{opt}}^{\text{min}} = \bar{d} - \frac{1}{3} \Delta d$. $\Delta d = |d_{\text{opt}}^{\text{max}} - d_{\text{opt}}^{\text{min}}|$ is the maximum interlayer distance fluctuation which is easily obtained by first-principles calculations. Maximized interlayer distance is $d_{\text{opt}}^{\text{max}} = 3.60 \text{ \AA}$ with AA stacking and $d_{\text{opt}}^{\text{min}} = 3.35 \text{ \AA}$ with AB stacking.⁴⁴

Next, we determine the elastic ground state of TBG by minimizing the elastic potential energy. The minimized elastic potential energy can be determined by $\delta(U_E + U_B^{\parallel} + U_B^{\perp})/\delta\mathbf{u}^{(+)} = 0$ and $\delta(U_E + U_B^{\parallel} + U_B^{\perp})/\delta\mathbf{u}^{(-)} = 0$. Since the total potential energy is a semi-positive-definite function of $\mathbf{u}^{(+)}$, the ground-state energy $U_E + U_B^{\parallel} + U_B^{\perp}$ corresponds to $\mathbf{u}^{(+)} = 0$ and the total potential energy landscape only relies on $\mathbf{u}^{(-)}$. Figures 2(a)-(b) illustrates the potential energy landscapes before and after twisting, where warmer (colder) colors indicate higher (lower) local stacking energies. It is clearly observed that before and after twisting, the system undergoes spontaneous lattice relaxation, which can be treated as an adiabatic evolution process relative to the macroscopic system dynamics. Specifically, the AA stacking with high energy undergoes significant spatial shrink, whereas the AB/BA stacking with low energy undergoes significant spatial expansion, the corresponding displacement field of this process has been shown in Fig. 2(c). The complete 3D displacement field, encompassing both in-plane and out-of-plane relaxations, supports a topological Skyrmion number defined as

$$N = \frac{1}{4\pi} \iint_{\text{u.c.}} \mathbf{n} \cdot \left(\frac{\partial \mathbf{n}}{\partial x} \times \frac{\partial \mathbf{n}}{\partial y} \right) dx dy, \quad (3)$$

where $\mathbf{n} = \mathbf{u}^{(-)}/|\mathbf{u}^{(-)}|$ and spatial integration is restricted within one moiré unit cell. Since the unit direction field $\mathbf{n}(\mathbf{r})$ of each strain skyrmion is a localized, asymptotically uniform texture at

boundary, the two-dimensional plane can be one-point compactified to a sphere S^2 . As such, the skyrmion number is classified by the second homotopy group $\pi_2(S^2) = Z$, making it a quantized and topologically protected charge. This confirms the moiré strain texture is indeed a topological strain skyrmion in real space.

Our numerical calculation shows $N = +1$ for both clockwise and counter-clockwise twisting angles θ , but the resulting Skyrmions have different helicities depending on the sign of θ , i.e. chirality of the TBG. The topological number N does not rely on the values of Lamé coefficients λ and μ indicating interlayer twisting as a general way for emergent topological strain textures.

Strain Skyrmion Hall Effect

We investigate the dynamical properties of moiré strain Skyrmions in TBG under continuous interlayer sliding. The interlayer sliding can be simulated by replacing $\mathbf{u}^{(-)}$ by $\mathbf{u}^{(-)} + \mathbf{v}_0 t$ in the binding energy terms U_B^{\parallel} and U_B^{\perp} , with \mathbf{v}_0 representing the interlayer sliding velocity, i.e.

$$\begin{aligned}
 U_B^{\parallel} &\rightarrow \tilde{U}_B^{\parallel} = \int d^2\mathbf{r} \sum_{j=1}^3 V_0 \cos[\mathbf{G}_j^M \cdot \mathbf{r} + \mathbf{a}_j^* \cdot (\mathbf{u}^{(-)} + \mathbf{v}_0 t)], \\
 U_B^{\perp} &\rightarrow \tilde{U}_B^{\perp} = \int d^2\mathbf{r} C[u_z^{(-)} + \bar{d} - \tilde{d}_{\text{opt}}]^2, \\
 \tilde{d}_{\text{opt}} &= \bar{d} + \sum_{j=1}^3 \frac{2}{9} \Delta d \cos[\mathbf{G}_j^M \cdot \mathbf{r} + \mathbf{a}_j^* \cdot (\mathbf{u}^{(-)} + \mathbf{v}_0 t)].
 \end{aligned} \tag{4}$$

For a sufficiently small value of \mathbf{v}_0 , the effect of this relative displacement can be approximately treated as an adiabatic process. For a horizontal interlayer sliding $\mathbf{v}_0 = v_0 \hat{\mathbf{e}}_x$ with $v_0 = 0.1 \text{ \AA/s}$, the time evolution of the ground-state distribution of $\mathbf{u}^{(-)}$ determined by $\delta(U_E + \tilde{U}_B^{\parallel} + \tilde{U}_B^{\perp})/\delta\mathbf{u}^{(-)} = 0$ is shown in Fig. 3(a), more examples can be seen in Supplemental Material.⁴⁵ We find that at a generic time t the distribution of $\mathbf{u}^{(-)}$ is still a strain Skyrmion with $N = +1$. As t increases, the strain Skyrmion centers move vertically with constant speed v_s indicating an interlayer sliding driven strain Skyrmion Hall effect.

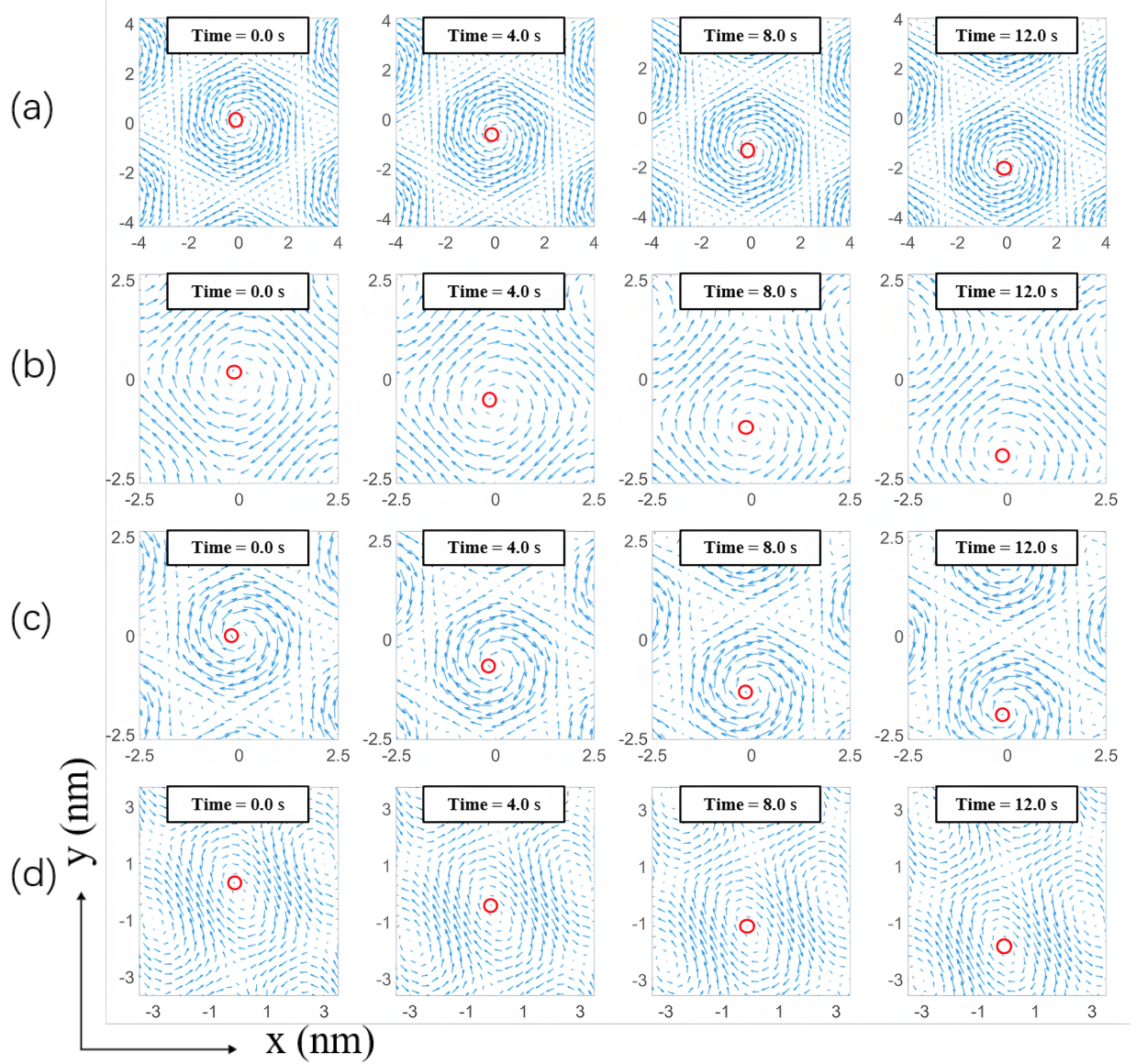


Figure 3: Vortex motion induced by inter-layer sliding in moiré bilayers with different point group symmetries. (a) Motion of vortex induced by sliding with C_6 symmetry. (b)-(d) Same as (a) but with point group symmetries C_4 , C_3 , and C_2 , respectively. The elastic parameters λ , μ , V_0 are taken as same as TBG. The red circles indicate the vortex centers.

Such a sliding driven strain Skyrmion Hall effect generally exist in two-dimensional moiré systems with point group symmetries C_n ($n = 2, 3, 4, 6$). The binding energy density $\mathcal{U}_B^\parallel, \mathcal{U}_B^\perp$ is constructed as

$$\begin{aligned}\mathcal{U}_B^\parallel &= \int d^2\mathbf{r} \sum_{j=1}^n V_0 \cos[\mathbf{G}^M \cdot \mathbf{r}' + \mathbf{a}^* \cdot (\mathbf{u}^{(-)'} + \mathbf{v}_0 t)], \\ \mathcal{U}_B^\perp &= \int d^2\mathbf{r} C[u_z^{(-)} + \bar{d} - \tilde{d}'_{\text{opt}}], \\ \tilde{d}'_{\text{opt}} &= \bar{d} + \sum_{j=1}^n \frac{2}{9} \Delta d \cos[\mathbf{G}^M \cdot \mathbf{r}' + \mathbf{a}^* \cdot (\mathbf{u}^{(-)'} + \mathbf{v}_0 t)],\end{aligned}\tag{5}$$

where $\mathbf{r}' = C_n^{-j}\mathbf{r}$ and $\mathbf{u}^{(-)'} = C_n^j\mathbf{u}^{(-)}(C_n^{-j}\mathbf{r})$ represent the rotation transformation of \mathbf{r} and $\mathbf{u}^{(-)}(\mathbf{r})$, respectively. $C_n^j = R_z(2\pi j/n)$ is the rotation symmetry operation. \mathbf{a}^* and \mathbf{G}^M represents one of the reciprocal Bravais lattice vector for the primitive monolayer and its corresponding moiré bilayer. Figures 3(b)-(d) show the time evolution of strain vortex for $n = 4, 3, 2$, respectively. Two conclusions can be drawn: (i) The strain Skyrmion is the ground state of moiré system with arbitrary rotational symmetry C_n ; (ii) In the presence of interlayer sliding, the strain Skyrmion lattices generally exhibit Hall effect with similar Hall drift velocity.

In order to quantitatively describe the strain Skyrmion Hall effect, we rewrite the argument in the first and third lines of Eq. (5) as

$$\mathbf{G}^M \cdot \mathbf{r} + \mathbf{a}^* \cdot (\mathbf{u}^{(-)} + \mathbf{v}_0 t) = \mathbf{G}^M \cdot (\mathbf{r} - \mathbf{v}_s t) + \mathbf{a}^* \cdot \mathbf{u}^{(-)}.\tag{6}$$

The above equation indicates that the relative interlayer sliding $\mathbf{v}_0 t$ can be equivalent to the movement of strain field $\mathbf{u}^{(-)}(\mathbf{r})$ by replacing \mathbf{r} by $\mathbf{r} - \mathbf{v}_s t$. \mathbf{v}_s is the moving velocity of the strain field. Combining Eq. (6) with the relation $\mathbf{G}_j^M = [1 - R_z(-\theta)]\mathbf{a}_j^*$, we can derive that

$$\mathbf{v}_s = - \{[1 - R_z(-\theta)]^\top\}^{-1} \mathbf{v}_0 = \frac{1}{\theta} \begin{pmatrix} 0 & 1 \\ -1 & 0 \end{pmatrix} \mathbf{v}_0 + O(\theta^2).\tag{7}$$

For small value of θ , the Skyrmion velocity \mathbf{v}_s is proportional to sliding velocity \mathbf{v}_0 . We define the Skyrmion Hall angle θ_H as $\theta_H \equiv |\mathbf{v}_s|/|\mathbf{v}_0| = 1/\theta$. That is, the smaller twist angle θ is the larger the Skyrmion Hall angle θ_H is. It is interesting to note that the Skyrmion Hall angle only depends on the twist angle θ but does not rely on other details of the moiré lattice.

To quantitatively verify the accuracy of the numerical simulation calculations, we compared the Skyrmion Hall angle θ_H with various twist angle θ , and compared these numerical results with the theoretical velocity values derived from Equation (7). The results are shown in Fig. 4 and exhibit a remarkable high goodness of fit, confirming that our numerical simulations perfectly capture the theoretical topological kinematics within the margin of error.

Our results demonstrate that moiré systems across all tested symmetries exhibit this linear topological Hall effect, underscoring the universality of the kinematic law. Fundamentally, this process can be mapped onto a mechanical Thouless pumping mechanism,^{46,47} because after completing a full spatial period of interlayer sliding, the topological skyrmions are discretely pumped by a precisely quantized transverse displacement.

Discussion

The fundamental upper bound of v_s is limited by the lattice relaxation time, or the average phonon lifetime τ_{ph} , which is typically at the order of picoseconds. Generally, a smaller τ_{ph} allows a faster relaxation of the strained lattice and thus a higher upper bound of v_s . Take $\tau_{ph} = 1$ ps,⁴⁸⁻⁵⁰ the adiabatic condition requires that $v_s \ll \max\{|\mathbf{u}^{(-)}|\}/\tau_{ph} \approx 32$ m/s, where $\max\{|\mathbf{u}^{(-)}|\} = 0.32$ Å is the maximum value of $|\mathbf{u}^{(-)}(\mathbf{r})|$ in magic angle TBG. Furthermore, the interlayer sliding can further reduce the phonon lifetime τ_{ph} due to interlayer friction⁵¹⁻⁵³ which favors an even larger upper bound of v_s and Skyrmion Hall angle θ_H . Given that phonon relaxation timescales are typically much shorter than the timescales of macroscopic mechanical manipulation, this dynamical limit warrants further experimental investigation^{3,51,52} and phonon dynamical evolution.^{38,54}

In terms of the feasibility of the experiment, the purely mechanical origin of moiré strain

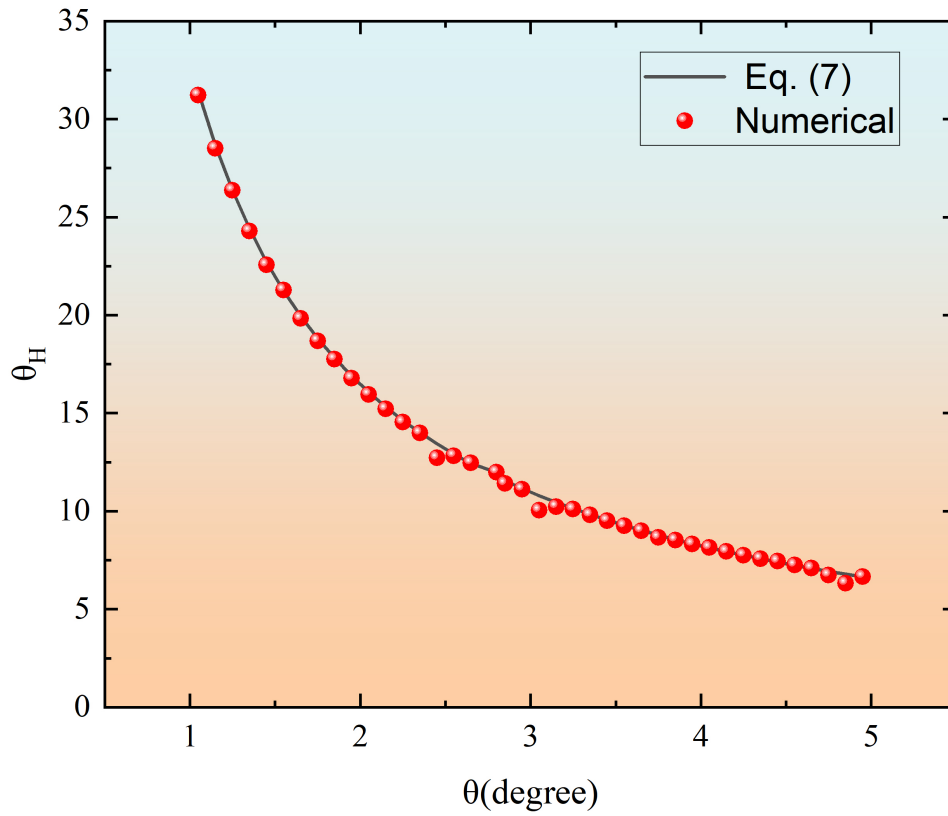


Figure 4: Comparison of theoretical values and numerical simulation results of the Skyrmion Hall angle $\theta_H = v_s/v_0$ as a function of twisting angle θ .

skyrmions enables straightforward observation and manipulation with state-of-the-art techniques. Scanning tunneling microscope (STM) can map sub-angstrom atomic displacements, which can directly resolve the 3D strain skyrmion lattice, while second-harmonic generation (SHG) microscopy enables fast large-area detection via strain-gradient-induced inversion symmetry breaking.⁵⁵ Also, interlayer sliding can be achieved by contact-mode AFM tips,^{53,56} allowing deterministic control of individual skyrmions. Applying AFM to track skyrmion center trajectories in real time can directly quantify the Hall angle. Notably, unlike magnetic skyrmions which requires magnetic fields or currents with Joule heating, electronic skyrmions which requires cryogenic temperatures, and ferroelectric skyrmions which are limited to polar materials, strain skyrmions operate at room temperature with negligible dissipation and are universal to all twisted van der Waals bilayers with C_n symmetry.⁵⁷

Furthermore, in sliding ferroelectric moiré systems, lattice relaxation could be considered as electric dipoles and facilitates the modulation of the moiré potential energy, thereby controlling the moiré ferroelectric domains and regulating their thermal stability,^{58,59} thus this demonstrates that strain defects specifically via interlayer sliding—can serve as a powerful, purely mechanical control knob for manipulating skyrmions across both van der Waals heterostructures and sliding ferroelectric systems.

Conclusion

In summary, utilizing a continuum elastic model system under the process of adiabatic evolution, we have systematically investigated the relaxation of in-plane and out-of-plane structural displacement fields in twisted bilayer graphene. We demonstrate that this mechanical relaxation naturally gives rise to stable, three-dimensional strain skyrmions in real space. Furthermore, by introducing continuous interlayer sliding, we discover that these skyrmions exhibit a highly controllable, transverse linear Hall effect. By generalizing our model to encompass various 2D chiral point group symmetries, we have proven the universality of this purely mechanical topological pumping mech-

anism. We have obtained consistent conclusions across different chiral twisted systems. These findings provide a robust theoretical foundation for the mechanical manipulation of topological quasiparticles, potentially opening new avenues for the design of novel chiral material devices and high-speed, mechanically driven information transport architectures.

Acknowledgments

We thank Yang Long for stimulating discussions. This work is supported by the National Natural Science Foundation of China (Grant No. 12404279), the Quantum Science and Technology-National Science and Technology Major Project (Grant No. 2023ZD0300500), and the National Key R&D Program of China (Grant Nos. 2023YFA1406900 and 2022YFA1404400).

References

- (1) Nelson, D. R. *Defects and geometry in condensed matter physics*; Cambridge University Press, 2002.
- (2) Castro Neto, A. H.; Guinea, F.; Peres, N. M. R.; Novoselov, K. S.; Geim, A. K. The electronic properties of graphene. *Rev. Mod. Phys.* **2009**, *81*, 109–162.
- (3) Hou, Y.; Zhou, J.; Xue, M.; Yu, M.; Han, Y.; Zhang, Z.; Lu, Y. Strain Engineering of Twisted Bilayer Graphene: The Rise of Strain-Twistronics. *Small* **2025**, *21*, 2311185.
- (4) Dai, Z.; Liu, L.; Zhang, Z. Strain Engineering of 2D Materials: Issues and Opportunities at the Interface. *Adv. Mater.* **2019**, *31*, 1805417.
- (5) Feng, J.; Qian, X.; Huang, C.-W.; Li, J. Strain-engineered artificial atom as a broad-spectrum solar energy funnel. *Nat. Photonics* **2012**, *6*, 866–872.
- (6) Peng, Z.; Chen, X.; Fan, Y.; Srolovitz, D. J.; Lei, D. Strain engineering of 2D semiconductors

- and graphene: from strain fields to band-structure tuning and photonic applications. *Light Sci. Appl.* **2020**, *9*, 190.
- (7) Si, C.; Sun, Z.; Liu, F. Strain engineering of graphene: a review. *Nanoscale* **2016**, *8*, 3207–3217.
- (8) Yazyev, O. V.; Louie, S. G. Topological defects in graphene: Dislocations and grain boundaries. *Physical Review B—Condensed Matter and Materials Physics* **2010**, *81*, 195420.
- (9) Stukowski, A.; Albe, K. Extracting dislocations and non-dislocation crystal defects from atomistic simulation data. *Modelling and Simulation in Materials Science and Engineering* **2010**, *18*, 085001.
- (10) Hull, D.; Bacon, D. J. *Introduction to dislocations*; Elsevier, 2011; Vol. 37.
- (11) Freysoldt, C.; Grabowski, B.; Hickel, T.; Neugebauer, J.; Kresse, G.; Janotti, A.; Van de Walle, C. G. First-principles calculations for point defects in solids. *Rev. Mod. Phys.* **2014**, *86*, 253–305.
- (12) Macdonald, D. D. The Point Defect Model for the Passive State. *Journal of The Electrochemical Society* **1992**, *139*, 3434.
- (13) The history of the Point Defect Model for the passive state: A brief review of film growth aspects. *Electrochimica Acta* **2011**, *56*, 1761–1772, ADVANCES IN CORROSION SCIENCE FOR LIFETIME PREDICTION AND SUSTAINABILITY Selection of papers from the 8th ISE Spring Meeting 2-5 May 2010, Columbus, OH, USA.
- (14) Wei, Y.; Wu, J.; Yin, H.; Shi, X.; Yang, R.; Dresselhaus, M. The nature of strength enhancement and weakening by pentagon–heptagon defects in graphene. *Nature materials* **2012**, *11*, 759–763.
- (15) Koma, A. Van der Waals epitaxy for highly lattice-mismatched systems. *Journal of Crystal Growth* **1999**, *201-202*, 236–241.

- (16) Liu, J.; Zhang, J. Nanointerface Chemistry: Lattice-Mismatch-Directed Synthesis and Application of Hybrid Nanocrystals. *Chemical Reviews* **2020**, *120*, 2123–2170, PMID: 31971378.
- (17) Si, C.; Liu, Z.; Duan, W.; Liu, F. First-Principles Calculations on the Effect of Doping and Biaxial Tensile Strain on Electron-Phonon Coupling in Graphene. *Phys. Rev. Lett.* **2013**, *111*, 196802.
- (18) Sarkar, S.; Ren, X.; Otsuka, K. Evidence for strain glass in the ferroelastic-martensitic system Ti 50-x Ni 50+ x. *Phys. Rev. Lett.* **2005**, *95*, 205702.
- (19) Wang, D.; Zhang, Z.; Zhang, J.; Zhou, Y.; Wang, Y.; Ding, X.; Wang, Y.; Ren, X. Strain glass in Fe-doped Ti–Ni. *Acta Mater.* **2010**, *58*, 6206–6215.
- (20) Wang, Y.; Ren, X.; Otsuka, K. Shape memory effect and superelasticity in a strain glass alloy. *Phys. Rev. Lett.* **2006**, *97*, 225703.
- (21) Xu, Z.; Ji, Y.; Liu, C.; He, L.; Zhao, H.; Yuan, Y.; Qian, Y.; Cui, J.; Xiao, A.; Wang, W.; others A polymer-like ultrahigh-strength metal alloy. *Nature* **2024**, *633*, 575–581.
- (22) Liu, W.; Ren, X. Large Piezoelectric Effect in Pb-Free Ceramics. *Phys. Rev. Lett.* **2009**, *103*, 257602.
- (23) Ren, X. Large electric-field-induced strain in ferroelectric crystals by point-defect-mediated reversible domain switching. *Nat. Mater.* **2004**, *3*, 91–94.
- (24) Zhang, J.; Mao, Y.; Wang, D.; Li, J.; Wang, Y. Accelerating ferroic ageing dynamics upon cooling. *NPG Asia Mater.* **2016**, *8*, e319–e319.
- (25) Long, Y.; Ren, J.; Chen, H. Intrinsic spin of elastic waves. *Proc. Natl. Acad. Sci.* **2018**, *115*, 9951–9955.
- (26) Shi, C.; Zhao, R.; Long, Y.; Yang, S.; Wang, Y.; Chen, H.; Ren, J.; Zhang, X. Observation of acoustic spin. *Natl. Sci. Rev.* **2019**, *6*, 707–712.

- (27) Long, Y.; Zhang, D.; Yang, C.; Ge, J.; Chen, H.; Ren, J. Realization of acoustic spin transport in metasurface waveguides. *Nat. Commun.* **2020**, *11*, 4716.
- (28) Long, Y.; Ge, H.; Zhang, D.; Xu, X.; Ren, J.; Lu, M.-H.; Bao, M.; Chen, H.; Chen, Y.-F. Symmetry selective directionality in near-field acoustics. *Natl. Sci. Rev.* **2020**, *7*, 1024–1035.
- (29) Yuan, W.; Yang, C.; Zhang, D.; Long, Y.; Pan, Y.; Zhong, Z.; Chen, H.; Zhao, J.; Ren, J. Observation of elastic spin with chiral meta-sources. *Nat. Commun.* **2021**, *12*, 6954.
- (30) Ren, J. From Elastic Spin to Phonon Spin: Symmetry and Fundamental Relations. *Chinese Phys. Lett.* **2022**, *39*, 126301.
- (31) Yang, C.; Zhang, D.; Zhao, J.; Gao, W.; Yuan, W.; Long, Y.; Pan, Y.; Chen, H.; Nori, F.; Bliokh, K. Y.; Zhong, Z.; Ren, J. Hybrid Spin and Anomalous Spin-Momentum Locking in Surface Elastic Waves. *Phys. Rev. Lett.* **2023**, *131*, 136102.
- (32) Yang, C.; Ren, J. Chirality-induced phonon spin selectivity by elastic spin–orbit interaction. *Proc. Natl. Acad. Sci.* **2024**, *121*, e2411427121.
- (33) Liu, Y.; Lian, C.-S.; Li, Y.; Xu, Y.; Duan, W. Pseudospins and Topological Effects of Phonons in a Kekulé Lattice. *Phys. Rev. Lett.* **2017**, *119*, 255901.
- (34) Budich, J. C.; Dolcini, F.; Recher, P.; Trauzettel, B. Phonon-Induced Backscattering in Helical Edge States. *Phys. Rev. Lett.* **2012**, *108*, 086602.
- (35) Liu, Y.; Xu, Y.; Duan, W. Berry phase and topological effects of phonons. *Nat. Sci. Rev.* **2018**, *5*, 314–316.
- (36) Liu, Y.; Chen, X.; Xu, Y. Topological Phononics: From Fundamental Models to Real Materials. *Adv. Funct. Mater.* **2020**, *30*, 1904784.
- (37) Liu, Y.; Zou, N.; Zhao, S.; Chen, X.; Xu, Y.; Duan, W. Ubiquitous topological states of phonons in solids: Silicon as a model material. *Nano Lett.* **2022**, *22*, 2120–2126.

- (38) Lei, C.; Wang, Z.; Yang, C.; Liu, Y.; Ren, J. Quantum Phononics: From Principles to Engineering. *J. Phys. Chem. Lett.* **2025**, *16*, 7630–7641.
- (39) Zhao, J.; Yang, C.; Yuan, W.; Zhang, D.; Long, Y.; Pan, Y.; Chen, H.; Zhong, Z.; Ren, J. Elastic valley spin controlled chiral coupling in topological valley phononic crystals. *Phys. Rev. Lett.* **2022**, *129*, 275501.
- (40) Liu, Y.; Xiao, J.; Koo, J.; Yan, B. Chirality-driven topological electronic structure of DNA-like materials. *Nat. Mater.* **2021**, *20*, 638–644.
- (41) Koshino, M.; Son, Y.-W. Moiré phonons in twisted bilayer graphene. *Phys. Rev. B* **2019**, *100*, 075416.
- (42) Nam, N. N. T.; Koshino, M. Lattice relaxation and energy band modulation in twisted bilayer graphene. *Phys. Rev. B* **2017**, *96*, 075311.
- (43) Suri, N.; Wang, C.; Zhang, Y.; Xiao, D. Chiral Phonons in Moiré Superlattices. *Nano Lett.* **2021**, *21*, 10026–10031.
- (44) Lin, X.; Liu, D.; Tománek, D. Shear instability in twisted bilayer graphene. *Phys. Rev. B* **2018**, *98*, 195432.
- (45) Supporting Information.
- (46) Thouless, D. J. Quantization of particle transport. *Phys. Rev. B* **1983**, *27*, 6083–6087.
- (47) Zhang, Y.; Gao, Y.; Xiao, D. Topological charge pumping in twisted bilayer graphene. *Phys. Rev. B* **2020**, *101*, 041410(R).
- (48) Nika, D. L.; Balandin, A. A. Phonons and thermal transport in graphene and graphene-based materials. *Rep. Prog. Phys.* **2017**, *80*, 036502.
- (49) Bonini, N.; Garg, J.; Marzari, N. Acoustic Phonon Lifetimes and Thermal Transport in Free-Standing and Strained Graphene. *Nano Lett.* **2012**, *12*, 2673–2678.

- (50) Chen, L.; Kumar, S. Thermal transport in graphene supported on copper. *J. Appl. Phys.* **2012**, *112*.
- (51) Koren, E.; Duerig, U. Moiré scaling of the sliding force in twisted bilayer graphene. *Phys. Rev. B* **2016**, *94*, 045401.
- (52) Minkin, A. S.; Lebedeva, I. V.; Popov, A. M.; Vyrko, S. A.; Poklonski, N. A.; Lozovik, Y. E. Restriction of macroscopic structural superlubricity due to structure relaxation by the example of twisted graphene bilayer. *Phys. Rev. Mater.* **2025**, *9*, 024002.
- (53) Koren, E.; Lörtscher, E.; Rawlings, C.; Knoll, A. W.; Duerig, U. Adhesion and friction in mesoscopic graphite contacts. *Science* **2015**, *348*, 679–683.
- (54) Wang, Z.; Ren, J. Thermodynamic Geometry of Nonequilibrium Fluctuations in Cyclically Driven Transport. *Phys. Rev. Lett.* **2024**, *132*, 207101.
- (55) Yang, F.; Song, W.; Meng, F.; Luo, F.; Lou, S.; Lin, S.; Gong, Z.; Cao, J.; Barnard, E. S.; Chan, E.; others Tunable second harmonic generation in twisted bilayer graphene. *Matter* **2020**, *3*, 1361–1376.
- (56) Jiang, L.; Wang, S.; Shi, Z.; Jin, C.; Utama, M. I. B.; Zhao, S.; Shen, Y.-R.; Gao, H.-J.; Zhang, G.; Wang, F. Manipulation of domain-wall solitons in bi-and trilayer graphene. *Nat. Nanotechnol.* **2018**, *13*, 204–208.
- (57) Li, L.; Wu, M. Binary Compound Bilayer and Multilayer with Vertical Polarizations: Two-Dimensional Ferroelectrics, Multiferroics, and Nanogenerators. *ACS Nano* **2017**, *11*, 6382–6388.
- (58) Li, L.; Wu, M. Binary Compound Bilayer and Multilayer with Vertical Polarizations: Two-Dimensional Ferroelectrics, Multiferroics, and Nanogenerators. *ACS Nano* **2017**, *11*, 6382–6388.

- (59) Zheng, Z.; Ma, Q.; Bi, Z.; de La Barrera, S.; Liu, M.-H.; Mao, N.; Zhang, Y.; Kiper, N.; Watanabe, K.; Taniguchi, T.; others Unconventional ferroelectricity in moiré heterostructures. *Nature* **2020**, 588, 71–76.

TOC Graphic

